PHYSICAL REVIEW B **92**, 184109 (2015)

Phase-field crystal approach for modeling the role of microstructure in multiferroic composite materials

Matthew Seymour,[1] F. Sanches,[2] Ken Elder,[2] and Nikolas Provatas[1]
[1]*Department of Physics, Centre for the Physics of Materials, McGill University, Montreal, QC, Canada*
[2]*Department of Physics, Oakland University, Rochester, Michigan 48309, USA*
(Received 13 July 2015; published 23 November 2015)

This paper introduces a phase-field crystal (PFC) approach that couples the atomic-scale PFC density field to order parameters describing ferromagnetic and ferroelectric ordering, as well to a solute impurity field. This model extends the magnetic PFC model introduced by Faghihi *et al.* [N. Faghihi, Ph.D. Thesis, The University of Western Ontario, 2012; N. Faghihi, N. Provatas, K. R. Elder, M. Grant, and M. Karttunen, Phys. Rev. E **88**, 032407 (2013)] to incorporate polarization and concentration fields, as well as anisotropic ordering of the magnetization and polarization fields as determined by the local crystalline orientation. Magnetoelectric coupling is incorporated through the elastic coupling. Analytic calculations for a body centered-cubic (BCC) system are presented to illustrate that the model reduces to the standard multiferroic phase-field models when only a single crystal is considered. Two special cases of the model are then studied, the first focusing on magnetocrystalline interactions in a system described by the two-point correlation function of the XPFC model developed by Greenwood *et al.* [M. Greenwood, N. Provatas, and J. Rottler, Phys. Rev. Lett. **105**, 045702 (2010); M. Greenwood, J. Rottler, and N. Provatas, Phys. Rev. E **83**, 031601 (2011)], and the second focusing on electrocrystalline interactions in a system described by the original PFC kernel developed by Elder *et al.* K. R. Elder, M. Katakowski, M. Haataja, and M. Grant, Phys. Rev. Lett. **88**, 245701 (2002); K. R. Elder and M. Grant, Phys. Rev. E **70**, 051605 (2004)]. We examine the small deformation properties of these two realizations of the model . Numerical simulations are performed to illustrate how magnetocrystalline coupling can be exploited to design a preferential grain texture and how defects and grain boundaries influence the ferroelectric coercivity.

DOI: 10.1103/PhysRevB.92.184109 PACS number(s): 75.80.+q, 61.72.−y, 05.10.−a, 75.50.Tt

I. INTRODUCTION

When a solid undergoes a spontaneous transition to a magnetized or electrically polarized state, its emergent electromagnetic properties are strongly controlled by its microstructure because both the magnetization and polarization couple strongly to the crystalline structure of a material [1]. For example, the efficiency of a transformer core is directly influenced by its coercivity, which in turn is a function of the polycrystalline grain size [2–6]. This interaction is also vital to the control of flux lines in micromagnetic devices [7,8]. The emergence of a ferromagnetic or ferroelectric order can also induce a strain in the lattice. This effect is referred to as magnetostriction in the former case and the piezoelectricity in the latter. The coupling between electric, magnetic and elastic energy in materials has been exploited for many years. For example, the ability to turn magnetic or electric energy into mechanical energy and vice versa is the mechanism behind many sensors and actuators. Materials that contain at least two of the three properties, ferroelasticity, ferromagnetism, and ferroelectricity are referred to as multiferroic.

While there exist some single phase materials that are multiferroic typically these materials are unsuitable for practical applications as the magnetoelectric coupling is either too weak or occurs at low temperatures [9]. In recent years, researchers have been considering composite materials which contain both ferromagnetic and ferroelectric properties (e.g., $YMnO_3$ and $BaNiGF_4$) [10–12]. Such materials are of great interest as the elastic coupling between the materials can be exploited by using either a magnetic field to control ferroelectricity or an electric field to control magnetization. The latter is particularly attractive for nonviotile memory applications in semiconductors where the ability to write and read on a magnetic material using an electric field is very advantageous. Heteroepitaxially grown films offer a promising configuration for such composite materials, although the great costs associated with their fabrication makes them difficult and expensive to realize. For this reason, there is a need to understand the properties of self-assembled multiferroic materials made by cost effective processes like sintering, embedding particles of one material in another or eutectic solidification [13–15]. The purpose of this work is to develop a model of a binary polycrystalline multiferroic material that can elastically couple the magnetism of one material to the polarization of the other though the magnetostriction and piezoelectric effects.

Modelling multiferroic material properties is challenging because magnetization and polarization couple strongly to the microstructure of a material. For example, the crystal lattice often determines the direction in which the magnetic ($\vec{m}$) or electric ($\vec{P}$) dipoles align. However, in a real materials, each grain typically has a different crystallographic orientation. This grain texture can significantly alter coercivity in polycrystalline materials [2–6], a measure of the strength of the external magnetic field needed to change the direction of magnetization in the material. Furthermore, the presence of grain boundaries, dislocations and magnetic impurities is also expected to influence magnetization and polarization, either directly or through the influence of such topological defects on grain size. In addition, it is expected that the volume fraction of composite components or phases also will be important.

Another difficulty in modeling multiferroics is due to the multiple length and time scales that need to be considered.

Molecular dynamics simulations offer an accurate way to simulate atomic interactions. However, they are often limited to nanoseconds time scales and nanometer length scales. Traditional phase-field models describe multiferroics by a free energy functional that couples polarization, magnetization and strain. Phase field models are simple to implement numerically, can access mesoscopic time and length scales [16] and are amenable to highly scalable computational algorithms [17,18]. These models incorporate anisotropy with respect to an *a priori* known crystal orientation and elasticity through the introduction of additional fields. For example, the Landau-Ginzburg-Devonshire free energy [19] for ferroelectrics includes terms like $\alpha_{11}\sum P_i^4 + \alpha_{12}\sum_{j>i} P_i^2 P_j^2$, where $\alpha_{12} \neq 2\alpha_{11}$ and i and j refer to cartesian coordinates. Grain orientation is incorporated by coupling polarization or magnetization to a local orientation parameter [20], which can be fixed from a grain distribution or, in principle, evolved according kinetic model. A drawback of traditional phase-field approaches is that they typically lack an explicit connection to atomic scale crystal structures.

An adaptation of the phase-field methodology that can help resolve some of the aforementioned modeling challenges is the phase-field crystal (PFC) model. PFC models are based on free energy functionals that can be minimized by periodic order parameters (e.g., triangular and square in two dimensions or body centered cubic (BCC), face centered cubic (FCC) and hexagonal closed packed (HPC) in three dimensions). The orientation of the order parameter in a crystal is arbitrary, i.e., the free energy F is written in a rotationally invariant manner. This feature endows PFC models with the ability to model elastic deformation, grain boundaries and topological defects in a self-consistent and straightforward manner [21–24]. The PFC order parameter is related to the atomic number density as PFC models can be viewed as approximations of classical density functional theory (CDFT) expanded to second order in particle correlations [23,26–28]. Recent PFC extensions have been used to capture complex structural transformations in pure materials [25,29–31] and multicomponent alloys [32,33]. These have been used to elucidate the physics of complex defect structures [34,35] and their role in solid state precipitation [36–38]. More recently, it has also been shown that it is possible to derive certain traditional phase-field models directly from PFC models through the use of course graining techniques [39,40]. This latter line of research allows meso-scale phenomena to be compter from the field models derived from microscopic PFC theories [39–43].

This paper introduces a binary multiferoic PFC model that couples the PFC crystal density field n and solute concentration field c to magnetization ($\vec{m}$) and polarization ($\vec{P}$) fields, making it possible to couple ferromagnetic/electric domain formation to grain orientation, grain boundaries, elastic strain, defects and solute impurities. The coupling of $\vec{m}$ and $\vec{P}$ with n at the atomic scale naturally leads to the emergence of magnetic/electric anisotropy at the mesoscale as well as the phenomena of magnetostriction and piezoelectricity. This model extends the work of Faghihi *et al.* [44,45], which considered a single component ferromagnetic PFC model without anisotropic ordering of $\vec{m}$. One of the important features of the model introduced here is that the form of coupling between $n, \vec{m}$, and $\vec{P}$ determines the preferred crystallographic directions in which $\vec{m}$ and $\vec{P}$ will order. This anisotropic ordering is a very important physical feature that has been used to explain the behavior of the magnetic coercivity in polycrystalline materials [2–5]. The model presented here does not consider the magnetoelectric coupling arising due to magnetic ordering heterogeneity, a phenomenon that occurs in some single phase materials at temperatures much lower than those of the multiferroic materials we wish to address with PFC modeling.

The remainder of this paper is organized as follows. Section II develops the model, describing its terms and parameters. Section III describes the dynamical equations of motion for $n, \vec{m}$, and $\vec{P}$. Section IV examines the model's equilibrium, anisotropic and small deformation elastic properties. To minimize repetitive algebra, these properties are explicitly derived only for the case of a ferro-magnetic system, since the algebra is analogous for the ferroelectric case. Section V examines two applications of the multiferroic PFC model. The first relates crystal grain size and electro-crystalline anisotropy to coercivity. The second demonstrates the role of external magnetic fields on grain orientation selection during coarsening. To further demonstrate the model's robustness, the first application utilizes involves the traditional PFC model and the second the structural, or XPFC model.

II. MODEL FORMULATION

This section introduces a free energy functional to model binary multiferroic polycrystalline materials. One of the guiding principles of the model is that its long-wavelength, small deformation limit reduces to traditional well-known phase-field theories, which have been very successful in describing ferromagnetic materials such as $CoFe_2O_4$ and ferroelectric materials such as $PbTiO_3$. Considering that the free energies of such traditional models can contain ten to twenty parameters, the proposed free energy will also require at minimum the same number of adjustable parameters. Connecting the parameters that enter the proposed model to these traditional free energies is discussed in latter sections of the text.

The proposed multiferroic PFC model is described by the following free energy functional:

$$\Delta F = \frac{\Delta \tilde{F}}{k_B T V \bar{\rho}} = \int d\vec{r}(f_{\rm id} + f_{\rm ex} + f_m + f_P + f_c), \qquad (1)$$

where $\tilde{F}$ represents the dimensional free energy, T denotes temperature, k_B the Boltzmann constant, and $\bar{\rho}$ some reference liquid density around which the free-energy functional is expanded. Each term in the integrand on the right is a free-energy density.

The terms $f_{\rm id}$ and $f_{\rm ex}$ in Eq. (1) are, respectively, the ideal and excess free energy of a polycrystalline system, represented by the reduced PFC density $n(\vec{r}) \equiv (\rho(\vec{r}) - \bar{\rho})/\bar{\rho}$, where $\rho(\vec{r})$ is related to the atomic number density of the material [24,46].

These terms are given by

$$f_{\mathrm{id}} = \frac{n^2}{2} - t\frac{n^3}{6} + v\frac{n^4}{12}, \tag{2}$$

$$f_{\mathrm{ex}} = -\frac{1}{2}n(\vec{r})\int C_2(|\vec{r}-\vec{r}\,'|)n(\vec{r}\,')d^3\vec{r}\,', \tag{3}$$

where t and v are constants that set the bulk free energy [25]. The function $C_2(|\vec{r}-\vec{r}\,'|)$ is the two point particle correlation function. Two specific forms of C_2 will be used in this paper. These and the remaining terms of Eq. (1) are discussed below.

A. Ferromagnetic components of free energy density

The term f_m is the magnetic free energy density, given by

$$f_m = \omega_B\left[\frac{W_0^2}{2}(\nabla\cdot\vec{m})^2 + (r_m - \omega_m n^2)\frac{|\vec{m}|^2}{2} + \gamma_m\frac{|\vec{m}|^4}{4} - \sum_{j=1}^{2}\frac{\alpha_{2j}}{2j}(\vec{m}\cdot\vec{\nabla}n)^{2j} - \vec{m}\cdot\vec{B} + \frac{|\vec{B}|^2}{2}\right], \tag{4}$$

where $\omega_B = B_0^2/(\mu_0 k_B T\bar{\rho})$ sets the scale of magnetic energy, with B_0 a reference magnetic field and μ_0 is the magnetic permeability of free space, and where $\vec{m}$ is the magnetization and $\vec{B}$ is the magnetic field (both in dimensionless units). The first term defines a generalized exchange energy gradient term, where the magnetic correlation length is modulated by the parameter W_0. The second and third terms are mean field type bulk free energy terms that control the ferromagnetic transition temperature. They first appeared in a recent isotropic version of the ferromagnetic PFC model model [45]. The variables r_m, ω_m, γ_m are constants related to the equilibrium magnetic energy of the material. The fourth term is new and couples the anisotropy of $\vec{m}$ to the crystal lattice through gradients of n, which select different orientation states in PFC models. The parameters α_2, α_4 (α_{2j}, $j = 1,2$) will be shown to control magnetorestriction and magnetic anisotropy in the in the model. The last two terms in f_m define the magnetostatic free energy.

B. Ferroelectric components of free energy density

The term f_P is the electric polarization free energy density, given by

$$f_P = \omega_E\left\{-G_2\frac{\vec{P}\cdot\nabla^2\vec{P}}{2} - G_1\frac{|\vec{\nabla}\times\vec{P}|^2}{2} + (r_p - \omega_p n^2)\frac{|\vec{P}|^2}{2} + \sum_j\left[\frac{\sigma_{2j}}{2j}|\vec{P}\cdot\nabla n|^{2j} + \frac{\beta_{2j}}{2j}|\vec{P}\times\nabla n|^{2j} + \frac{\nu_{2j}}{2j}|\vec{P}|^{2j}\right] + \frac{|\vec{E}|^2}{2}\right\}, \tag{5}$$

where $\omega_E = \epsilon_0 E_0^2/(k_B T\bar{\rho})$ sets the scale of the polarization energy, with E_0 a reference dimensional electric field and ϵ_0 is the permittivity of free space, and where $\vec{P}$ is the electrical polarization, $\vec{E}$ is the electric field (both in dimensionless units). The first and second terms on the right hand side of Eq. (5) control ferroelectric domain wall energy, where G_1 and G_2 are constants. The third term is added to control of the ferroelectric phase transition, where r_p and ω_p are constants. The fourth and fifth terms control anisotropy in polarization by coupling $\vec{P}$ to gradients in n through the constants σ_{2j} and β_{2j}. The sixth term makes it possible to include higher order bulk terms in $|\vec{P}|$, each controlled by the constants ν_{2j}. The last term in Eq. (5) is the electric dipole energy.

The ferromagnetic free energy has a simpler structure than the ferroelectric free energy for two reasons. First, for magnetic systems it is usually sufficient to describe the gradient energy with one exchange constant, thus requiring a lower order gradient expansion than the ferroelectric case, which requires higher order gradients combinations to accurately describe domain walls. Second, in ferromagnetic systems, a bulk free energy expansion of order $|\vec{m}|^4$ is typically sufficient (e.g., $CoFe_2O_4$ [47]). Ferroelectric systems, however, typically require higher order terms to describe experimental systems. For example, $PbTiO_4$ and $BaTiO_4$ have been described by sixth [48–50] and eighth [47] order polynomials in $\vec{P}$, respectively.

C. Alloy free energy density

The free energy density term f_c accounts for the free energy of impurities, described by a reduced concentration field $c(\vec{r}) \equiv C(\vec{r}) - \bar{C}$, where $C(\vec{r})$ is the ratio of the number density of impurity atom $\rho_B(\vec{r})$ to the total number density $\rho_A(\vec{r}) + \rho_B(\vec{r})$ and $\bar{C}$ is some reference concentration. The free energy density f_c is given by

$$f_c = \frac{1}{2}(a - bn^2)c^2 + \frac{c^4}{4} + \frac{K}{2}|\vec{\nabla}c|^2 + \frac{1}{2}(\alpha_m|\vec{m}|^2 - \alpha_P|\vec{P}|^2)\,c\,n^2, \tag{6}$$

where a, b, K, α_m and α_P are constants. The first three terms of f_c are the standard Cahn-Hilliard type terms that favor phase separation at a particular temperature, which depends on the average density through the n^2 term. The last term in f_c favors a ferroelectric state of an alloy when c is positive and a ferromagnetic state on an alloy when c is negative. More complex alloys are possible by using more sophisticated expansions. These will be examined elsewhere.

Table I shows the complete set of parameters appearing in the terms in the model.

D. Magnetostatics and electrostatics

The total magnetic field $\vec{B}$ (scaled by B_0) is given by

$$\vec{B} = \vec{B}_{\mathrm{ext}} + \vec{B}_{\mathrm{ind}}, \tag{7}$$

where $\vec{B}_{\mathrm{ext}}$ denotes any externally imposed magnetic field, while $\vec{B}_{\mathrm{ind}}$ is the induced magnetic field satisfying

$$\vec{B}_{\mathrm{ind}} = \vec{\nabla}\times\vec{A}, \tag{8}$$

$$\nabla^2\vec{A} = -\vec{\nabla}\times\vec{m}, \tag{9}$$

TABLE I. Model parameters for the ideal, ferromagnetic, ferroelectric, and alloy components of free energy.

Model parameters	
Ideal free energy parameters	
t,v	Sets the form of the ideal bulk free energy expansion [23,51,52]
Ferromagnetic parameters	
ω_B	Sets the scale of magnetic energy
W_0	Sets strength of the exchange interaction; controls domain wall width
r_m, ω_m, γ_m	Controls paramagnetic/ferromagnetic transition and sets the saturation magnetization
α_{2j}	Magnetostriction and anisotropy
Ferroelectric parameters	
ω_E	Sets the sale of polarization energy
G_1,G_2	Control domain wall energy
r_P, ω_P	Controls ferroelectric phase transition
σ_{2j}, β_{2j}	Piezoelectric effect and anisotropy
ν_{2j}	Control of higher order bulk $\vec{P}$ terms
Alloy parameters	
a, b	Control phase seperation
K	Compositional interface energy
α_m	Concentration dependence of magnetization
α_P	Concentration dependence of polarization

TABLE II. Model parameters for PFC and XPFC correlation functions.

Correlation function parameters	
PFC correlation function parameters	
ΔB	Temperature parameter
B^x	Elastic constant of the solid phase
XPFC correlation function parameters	
σ	Temperature parameter
i	Reciprocal space peak number
k_i	Reciprocal space peak wave number
β_i	Number of wave vectors in the ith family
ρ_i	Planar atomic density
ξ_i	Peak width; sets elastic constant

where $\vec{A}$ is the vector potential. The total electric field $\vec{E}$ (scaled by E_0) is given by

$$\vec{E} = \vec{E}_{\text{ext}} + \vec{E}_{\text{ind}}, \tag{10}$$

where $\vec{E}_{\text{ext}}$ denotes any externally imposed electric field, while $\vec{E}_{\text{ind}}$ is the dipole-induced electric field. It is described in terms of a potential field according to

$$E_{\text{ind}} = -\nabla\phi, \tag{11}$$

where ϕ is the electrostatic potential, given by the solution of

$$\nabla^2\phi = \nabla \cdot \vec{P}. \tag{12}$$

E. Two-point correlation functions

This work will examine the multiferroic model for two choices of two-point correlation functions. The first case specializes the correlation kernel in Eq. (3) to the single peak form in the original PFC model introduced by Elder *et al.* [21,24]. Written in Fourier space, this is given by

$$\hat{C}_2(q) = -\Delta B - 1 + B^x(1-q^2)^2, \tag{13}$$

where ΔB controls temperature and B^x the elastic constant of the solid phase [23]. This correlation function stabilizes triangular symmetry in 2D and body centered cubic (BCC) crystal structure in 3D. [21].

The second correlation function examined is the *XPFC* kernel introduced by Greenwood *et al.* [25,46], which is the envelope of multiple Gaussian peaks in Fourier space, of the form

$$\hat{C}_2^i(q) = e^{-\sigma^2 k_i^2/(2\rho_i\beta_i)}\, e^{-(q-k_i)^2/(2\xi_i^2)}, \tag{14}$$

where q denotes wave-number magnitude and i denotes a family of lattice planes with primary wave number k_i, which is referred to as the mode of the family i. The variable σ parameterizes temperature. The constants ξ_i, ρ_i, and β_i are, respectively, the ith Gaussian width (which sets the elastic constants along the $\vec{k}_i$ direction), the planar atomic density of the ith family of planes, and the number of planes in the ith family. Eq. (14) can stabilize triangular (2D) or BCC (3D) crystals if one peak is used, or square (2D) and face-centered-cubic (FCC -3D) if two peaks are used [25]. Table II summarizes the constants entering each of the two correlations above.

III. DYNAMICS OF $\vec{m}$, $\vec{P}$, n, AND c

The density n and concentration c are driven by conserved dynamics driven by fluxes proportional to the variation of the free energy with changes in each of these fields. Namely,

$$\frac{\partial n}{\partial t} = M_n \nabla^2\left(\frac{\delta F}{\delta n}\right), \tag{15}$$

$$\frac{\partial c}{\partial t} = M_c \nabla^2\left(\frac{\delta F}{\delta c}\right), \tag{16}$$

where M_n and M_c are used to set the time scale of solute versus total density diffusion. For a further separation of time scales between purely diffusive dynamics and quasielastic relaxation dynamics of n, an additional second order inertial time derivative is required on both these equations as has been illustrated in other works [22,53]. The magnetization and polarization follow nonconserved dynamics of the form

$$\frac{1}{\tau_m}\frac{\partial m_i}{\partial t} = -\frac{\delta F}{\delta m_i}, \tag{17}$$

$$\frac{1}{\tau_P}\frac{\partial P_i}{\partial t} = -\frac{\delta F}{\delta P_i}, \tag{18}$$

where τ_m and τ_P set the relaxation time scale of the magnetic and polarization fields, respectively. It is noteworthy that these dynamical equations for $\vec{m}$ are not the usual Landau-Lifshitz-Gilbert (LLG) type equations. The LLG equations are valid at microscopic time scales when the conservation of orbital angular momentum is relevant. On diffusional time scales studied with PFC models, $\vec{m}(\vec{r},t)$ represents a locally time averaged quantity, whose dynamics are driven by the minimization of a free energy.

It is instructive to write out explicitly the form of the dynamical equations for n, c, $\vec{m}$ and $\vec{P}$. For the density field,

$$\begin{aligned}\frac{\partial n}{\partial t} = M_n \nabla^2 \Bigg\{ n - \frac{t}{2}n^2 + \frac{v}{3}n^3 - \int C_2(|\vec{r}-\vec{r}'|)n(\vec{r}')\,d\vec{r}' + \omega_B[-\omega_m n m^2 + \alpha_2((\vec{m}\cdot\vec{\nabla}n)(\vec{\nabla}\cdot\vec{m}) + \vec{m}\cdot\vec{\nabla}(\vec{m}\cdot\vec{\nabla}n)) \\ + \alpha_4((\vec{m}\cdot\vec{\nabla}n)^3(\vec{\nabla}\cdot\vec{m}) + 3(\vec{m}\cdot\vec{\nabla}n)^2\vec{m}\cdot\vec{\nabla}(\vec{m}\cdot\vec{\nabla}n))] + (\alpha_m|\vec{m}|^2 - \alpha_P|\vec{P}|^2)c\,n - \omega_E\sum_j(\sigma_{2j}\vec{\nabla}\cdot[\vec{P}(\vec{P}\cdot\vec{\nabla}n)^{2j-1}] \\ + \beta_{2j}[|\vec{P}\times\vec{\nabla}n|^{2j-2}(\vec{\nabla}\times\vec{P})\cdot(\vec{P}\times\vec{\nabla}n) + (\vec{P}\times\vec{\nabla})\cdot|\vec{P}\times\vec{\nabla}n|^{2j-2}(\vec{P}\times\vec{\nabla}n)] + \omega_p n P^2 \Bigg\}\Bigg].\end{aligned} \tag{19}$$

For the concentration field,

$$\frac{\partial c}{\partial t} = M_c \nabla^2\left[(a - bn^2)c + c^3 - K\nabla^2 c + \frac{1}{2}(\alpha_m|\vec{m}|^2 - \alpha_P|\vec{P}|^2)n^2\right]. \tag{20}$$

For the components of the magnetization field,

$$\frac{1}{\tau_m}\frac{\partial m_i}{\partial t} = W_0^2\nabla^2 m_i - [r_m - (\omega_m - \alpha_m c)n^2 + \gamma_m|\vec{m}|^2]m_i + \alpha_2(\vec{m}\cdot\vec{\nabla}n)(\partial_i n) + \alpha_4(\vec{m}\cdot\vec{\nabla}n)^3(\partial_i n) + B_i. \tag{21}$$

For the components of the polarization field,

$$\begin{aligned}\frac{1}{\tau_P}\frac{\partial P_i}{\partial t} &= G_1\nabla^2 P_i + G_2(\vec{\nabla}\times(\vec{\nabla}\times\vec{P}))_i - (r_p - (\omega_p - \alpha_p c)n^2)P_i \\ &\quad + \sum_j[\sigma_{2j}(\vec{P}\cdot\vec{\nabla}n)^{2j-1}\vec{\nabla}n + \beta_{2j}|\vec{P}\times\vec{\nabla}n|^{2j-2}\,\vec{\nabla}n\times(\vec{P}\times\vec{\nabla}n) - \nu_{2j}|\vec{P}|^{2j-2}\vec{P}]_i + E_i.\end{aligned} \tag{22}$$

Equations (9) and (12) are solved at each time step of the dynamical evolution of n, c, m_i, P_i, $i = 1,2$ (2D).

Equations (19) to (22) represent relaxational dynamics on diffusional time scales, driven by a free-energy functional. As a result they require, in principle, a stochastic noise source to re-introduce the fluctuations washed out by the implied time averaging. As we will not be examining nucleation and interface fluctuations in this work, noise is left out of the dynamics.

IV. EQUILIBRIUM PROPERTIES OF MODEL

This section examines the equilibrium properties of the multiferroic PFC model, its anisotropy and its small deformation limit. To keep the algebra to a minimum, the mathematical steps of these derivations are shown explicitly only for the 3D ferromagnetic component of the model described by an XPFC correlation function. The mathematical steps are similar for the two types of models. The derivation of the piezoelectric coefficients in the ferroelectric model is also discussed, and results are shown for the case of the PFC correlation function.

A. Phase diagram

To represent the mean-field free energy of a solid phase in a PFC model, the density field $n(\vec{r})$ is expanded as a Fourier series over the appropriate Bravais lattice of the crystal phase being considered. This is given in a general form:

$$n(\vec{r}) = \sum_{\vec{q}_j} \eta_{\vec{q}_j} e^{i\vec{q}_j\cdot\vec{r}}, \tag{23}$$

where the sum is over all reciprocal lattice vectors $\vec{q}_j$ of the crystal. Reciprocal lattice vectors of the same length are said to belong to the same mode, indexed by k in what follows. We thus regroup the reciprocal lattice vectors by mode and reference them as $\vec{q}_j \to \vec{q}_{k,j}$. We similarly regroup the amplitudes and reference them as $\eta_{\vec{q}_j} \to \eta_{\vec{q}_{k,j}}$. Further, for simplicity, we take all the amplitudes in a mode to be equal and real, i.e., $\eta_{\vec{q}_{k,j}} = \phi_k$ for all j in the mode k. This assumption is sufficient for constructing the phase diagram of the system. With these considerations, Eq. (23) can be written as

$$n(\vec{r}) \approx \phi_0 + \sum_{k=1}^{N}\phi_k\left(\sum_{\vec{q}_{k,j}} e^{i\vec{q}_{k,j}\cdot\vec{r}}\right), \tag{24}$$

where N is the number of modes considered for a specific crystal structure of interest and ϕ_0 has been pulled out of the summation as this unique amplitude represents the average density of the system and is therefore fixed due to density conservation, serving as a parameter in the phase diagram.

The expansion of Eq. (24) is inserted into the free energy in Eq. (1), with the f_P and f_c contributions neglected for simplicity, as explained above. In the mean-field limit used to construct the phase diagram, terms of the form $e^{i(\vec{q}_i+\vec{q}_j+\ldots)\cdot\vec{r}}$ emerge, which integrate to zero unless $\vec{q}_i + \vec{q}_j + \ldots = 0$. This is known as a *resonance condition*. After integration, the resulting free energy will depend only on the amplitudes $\{\phi_k\}$, $\{m_i\}$, and the model parameters. We denote this mean field free energy as $F_{\rm mf}(\{\phi_k\},\{m_i\},\sigma)$.

To proceed, the mean-field free energy ($F_{\rm mf}$) is minimized with respect to each ϕ_k. This yields a set of ϕ_k as functions of ϕ_0, m_i, and σ. This minimization is done numerically. For simplicity, the $\vec{m}$-ϕ_k couplings are neglected in the determination of the ϕ_k. None of the results presented here change qualitatively, and the symbolic manipulation becomes

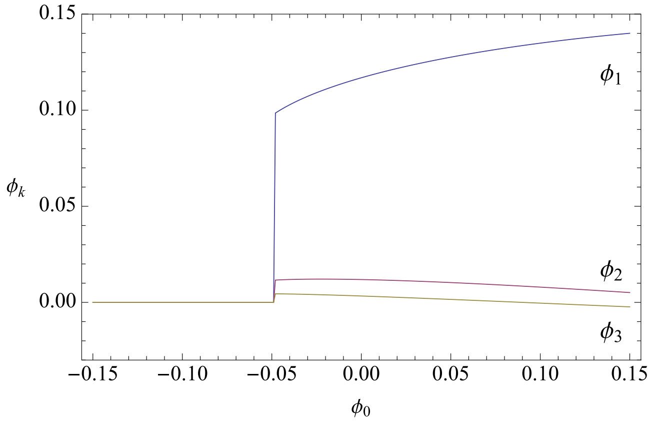

FIG. 1. (Color online) Amplitudes of the first three modes in Eq. (24) as a function of ϕ_0 for $\sigma = 0.12$ for the case of a single-peaked XPFC correlation with $k_1 = 2\sqrt{2}\pi$, $1/(2\rho_i\beta_i) = 1/24\sqrt{2}$, $t = v = 1$.

more tractable. Figure 1 plots the first three amplitudes of a BCC expansion versus ϕ_0 for the case of the single-peaked XPFC correlation kernel at $\sigma = 0.12$. We denote the $F_{\rm mf}$ evaluated at the minimized ϕ_k by ΔF.

Where the amplitudes are zero the free energy of the liquid is lower; where they are nonzero the solid free energy is lower. This abrupt transition to zero in the order parameters in Fig. 1 corresponds to a cusp in the system free energy. This is seen in Fig. 2, which plots ΔF versus ϕ_0. The cusp corresponds to the lowest possible average density at which a solid can exist.

Since ϕ_0 is a conserved order parameter, the coexistence region between the liquid and solid phases is found by the common tangent construction (or *Maxwell equal area construction*). Graphically, this amounts to finding the line that forms a common tangent to the convex parts of the free energy on either side of the cusp in Fig. 2. The tangent points define the average coexistence densities of the liquid and solid, respectively. These densities are found numerically.

To include more than one possible solid phase, an expansion of the form of Eq. (24) is written for each structure considered. In the present example, BCC and FCC solids are considered.

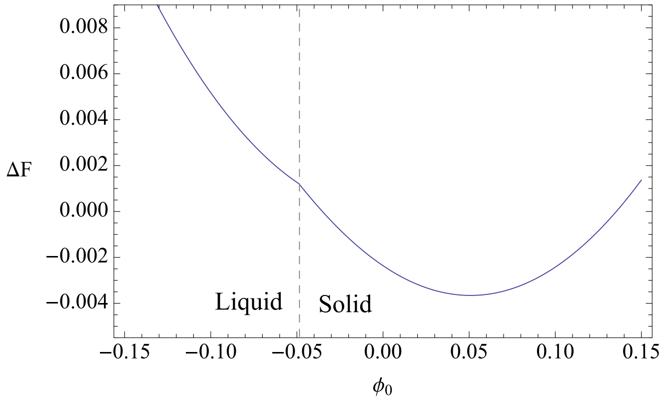

FIG. 2. (Color online) Free energy as a function of ϕ_0 for $\sigma = 0.12$. The other parameters are the same as described in Fig. 1. Note the kink at the liquid-solid transition.

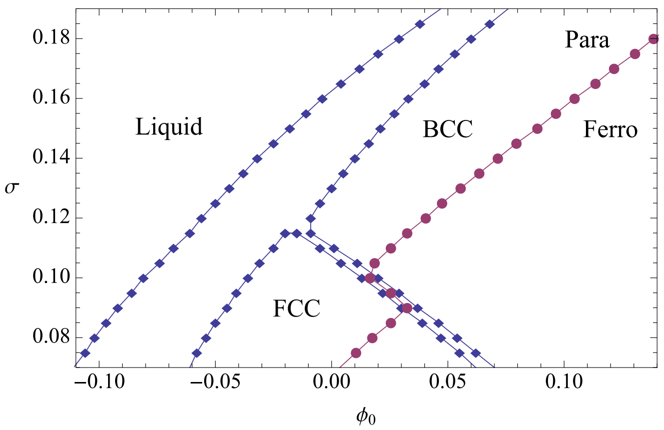

FIG. 3. (Color online) Phase diagram for the magneto-XPFC model, showing coexisting liquid, BCC and FCC phases, as well as paramagnetic and ferromagnetic phases. $\alpha_2 = 0.001$, $r_m = 0.025$, $\omega_m = 0.25$, $\gamma_m = 1$. Generated using five modes ($N = 5$).

Each expansion is substituted into the free energy to construct a mean-field free energy for that solid phase using the approach described above for a BCC crystal. At each temperature σ, the common tangent approach is used to define the coexistence lines between liquid and BCC, liquid and FCC, and BCC and FCC. Coexistence between any two phases will occur over a different range of ϕ_0. Calculating all such common tangent segments over a range of temperatures results in the complete phase diagram. An example is shown in Fig. 3 for a liquid-FCC-BCC system. This phase diagram corresponds to the model phase diagram first generated by Greenwood *et al.* [25,46] to describe FCC-BCC-liquid coexistence in the context of the XPFC model.

The paramagnetic-ferromagnetic transition line in Fig. 3 can be calculated for each solid phase using the solid amplitudes derived above. Specifically, the expansion in Eq. (24) leads to a magnetic part of the free energy of the form $Am^2 + Bm^4$, with a constant $B > 0$. When $A > 0$, a single minimum appears in the magnetic free energy density at $\vec{m} = 0$, which corresponds to paramagnetic ordering. When $A < 0$, the free energy is minimized at some $\vec{m} \neq 0$, corresponding to ferromagnetic ordering. For each solid phase, the factor A of the m^2 term depends on the mode amplitudes ϕ_k of the corresponding lattice, and the average density ϕ_0. For example, in the case of the single-peaked BCC correlation, the $|\vec{m}|^2$ term of the free energy becomes

$$\begin{aligned}\tfrac{1}{2}\big[r_m - \omega_m\phi_0^2 + \big(12k_1^2\alpha_2 - 12\omega_m\big)\phi_1^2 \\ + \big(12k_1^2\alpha_2 - 6\omega_m\big)\phi_2^2 + \big(72k_1^2\alpha_2 - 24\omega_m\big)\phi_3^2\big]|\vec{m}|^2,\end{aligned} \tag{25}$$

where $k_1 = |\vec{q}_{1,j}|$ is the length of the first set of reciprocal lattice vectors. Inserting the amplitudes (from Fig. 1) into the bracketed coefficient in Eq. (25) and setting it equal to zero gives the ferromagnetic transition line. This is illustrated in the phase diagram in Fig. 3. As mentioned above, the dependence of ϕ_k on $\vec{m}$ was neglected, which is exact at the paramagnetic/ferromagnetic transition line where $\vec{m} = 0$.

B. Magnetic anisotropy

Magnetic anisotropy is an essential feature in micromagnetic phenomena. In the literature, magnetic anisotropy is generally expressed with respect to specific orientations known as *easy axes*. As an example, for uniaxial anisotropy with symmetry along the z axis, the lowest-order anisotropic free energy per unit volume is given by

$$f_a = K_u m_z^2 \tag{26}$$

with the easy axis in the z direction for $K_u < 0$, otherwise for $K_u > 0$ there is an *easy plane* in the x-y plane. Cubic anisotropy with symmetry along the x, y, and z axes is given by

$$f_a = K_c\left(m_x^2 m_y^2 + m_x^2 m_z^2 + m_y^2 m_z^2\right) \tag{27}$$

with the easy axes along any of the six axes $\pm\hat{x}$, $\pm\hat{y}$, or $\pm\hat{z}$ for $K_c > 0$, or along any of the eight direction vectors $\pm\hat{x} \pm \hat{y} \pm \hat{z}$ for $K_c < 0$. The above forms cannot be used in the PFC free energy because the crystal orientation is not *a priori* known, since the free energy is rotationally invariant.

The simplest expression that contains information on the local crystal orientation is $\vec{\nabla} n$. In order to have magnetic anisotropy that depends on the local crystal orientation, only terms that couple $\vec{m}$ with $\vec{\nabla} n$ are included in the free energy. One type of coupling is of the form

$$\frac{1}{k}(\vec{m} \cdot \vec{\nabla} n)^k, \tag{28}$$

where k is some even integer. To obtain N-fold symmetry it is necessary (but not sufficient) that k be at least of order N. That is, to obtain twofold symmetry, $k = 2$, while for fourfold, $k = 4$, etc. Eq. (4) contains $\vec{m} \cdot \vec{\nabla} n$ coupling terms of order 2 and 4. The second-order term allows for uniaxial anisotropy in systems with HCP ordering. The fourth-order term allows for cubic anisotropy in BCC and FCC systems, as well as 2D square systems. Two-dimensional triangular systems require an additional sixth-order term.

To obtain an approximation of the long-wavelength form of the anisotropy energy contained in the $(\vec{m} \cdot \vec{\nabla} n)^k$ terms in Eq. (4), a single-mode expansion

$$n(\vec{r}) \approx \phi_0 + \sum_{\vec{q}_j} \phi e^{i\vec{q}_j \cdot \vec{r}} \tag{29}$$

is inserted into Eq. (28), where $\vec{q}_j$ are the lowest-order reciprocal lattice vectors of a crystal lattice. The result is

$$\frac{1}{k}\left(\sum_{\vec{q}_j}(i\vec{m} \cdot \vec{q}_j)\phi e^{i\vec{q}_j \cdot \vec{r}}\right)^k. \tag{30}$$

Expanding out Eq. (30) and applying the resonance condition (i.e., terms of the form $e^{i(\vec{q}_j + \vec{q}_k + \cdots + \vec{q}_l)\cdot\vec{r}}$ integrate to zero under coarse graining unless $\vec{q}_j + \vec{q}_k + \cdots + \vec{q}_l = 0$), an approximation of the anisotropic free energy in the phase field limit is obtained. For example, applying this procedure with $k = 4$ for a BCC lattice yields

$$\begin{aligned} f_a =& \frac{1}{V_u}\int d\vec{r}\left(-\frac{\alpha_4}{4}(\vec{m} \cdot \vec{\nabla} n)^4\right) \\ \approx& -\frac{27}{2}\alpha_4 (k_1 \phi \pi)^4 \left(|\vec{m}|^4 - \frac{7}{9}\left(m_x^2 m_y^2 + m_x^2 m_z^2 + m_y^2 m_z^2\right)\right), \end{aligned} \tag{31}$$

where the integration is over unit cell of volume $V_u = 1$. Note that since the result depends on the amplitude ϕ, the anisotropy depends on both the average density and the temperature parameter through the amplitude's dependance on these parameters. Equation (31) also ensures that anisotropy vanishes in the liquid region of the phase diagram.

The parameter α_4 can be either positive or negative in order to model different forms of anisotropy. Care must be taken, however, because for a large enough positive α_4, the coefficient of m^4 in Eq. (31) will exceed $\gamma_m/4$ and there will be no finite global minimum for the free energy as a function of $\vec{m}$. A similar issue exists with the ϕ^4 coefficient and the coarse grained term $vn^4/12$ in the free energy. To avoid these issues α_4 must either be sufficiently small, or terms higher order than fourth order in n must be added to f_{id}.

The above derivation considered only a liquid-BCC-FCC system. The XPFC formalism can also be used to model systems with HCP structure. Magnetically, these systems display uniaxial anisotropy. An approximation for this anisotropy is computed in an analogous manner as above, but now using the $(\vec{m} \cdot \nabla n)^2$ term, and taking into account the structure factors that arise due to the additional basis atom needed to describe HCP crystals. A single-mode expansion is not sufficient in this case. The lowest-order (smallest $\vec{q}$) mode of the underlying hexagonal Bravais lattice vanishes when the structure factor of the two atom basis is computed. The next lowest-order mode lies in the basal plane; we denote it's amplitude with ϕ. With these modifications to Eq. (29), the phase-field limit of the α_2 term becomes

$$-\frac{\alpha_2}{2}(\vec{m} \cdot \vec{\nabla} n)^2 \approx -\frac{4}{3}\alpha_2 \phi^2 k_1^2\left(|\vec{m}|^2 - m_z^2\right), \tag{32}$$

which is consistent with the form for uniaxial anisotropy.

C. Small deformation limit

Phase-field crystal models contain a natural elastic response. An interesting consequence of magnetocrystalline interactions is the capacity of crystal phases to deform in the presence of a magnetic field. This effect is known as magnetostriction in ferromagnetic materials and the piezoelectric effect in ferroelectric materials. This section derives the magnetostriction and piezoelectric coefficients of the present model.

Before proceeding, the density expansion is simplified by assuming that the amplitudes are complex and can vary in space, i.e.,

$$n(\vec{r}) = \sum_{\vec{q}_j} \eta_{\vec{q}_j}(\vec{r}) e^{i\vec{q}_j \cdot \vec{r}}. \tag{33}$$

The amplitudes are then decomposed in the form of a real magnitude and complex phase, specifically,

$$\eta_{\vec{q}_j}(\vec{r}) = \phi_{\vec{q}_j} e^{i\vec{q}_j\cdot\vec{u}(\vec{r})}. \tag{34}$$

where $\vec{u}(\vec{r})$ is a displacement field that serves to strain the system. Inserting Eq. (34) into Eq. (33) yields

$$n(\vec{r}) = \sum_{\vec{q}_j} \phi_{\vec{q}_j} e^{i\vec{q}_j\cdot(\vec{u}(\vec{r})+\vec{r})}. \tag{35}$$

We denote the spatial derivatives of $\vec{u}(\vec{r})$ as $\partial_{r_j} u_i = u_{ij}$ $(i = 1,2,3)$. Expanding $\vec{u}(\vec{r})$ about a reference position in the deformed material makes it possible to write $u_i(\vec{r}) = \sum_j u_{ij} r_j$, in the small deformation limit. Then, by defining $q'_j = q_i u_{ij}$, Eq. (35) can be re-expressed as

$$n(\vec{r}) = \sum_{\vec{q}_j} \phi_{\vec{q}_j} e^{i(\vec{q}_j+\vec{q}\,'_j)\cdot\vec{r}}. \tag{36}$$

In reciprocal space, Eq. (36) becomes

$$\hat{n}(\vec{k}) = \sum_{\vec{q}_j} \phi_{\vec{q}_j} \delta((\vec{q}_j + \vec{q}\,'_j) - \vec{k}). \tag{37}$$

Equation (37) is used below to compute contributions to the elastic energy arising from the relevant terms in the PFC free energy.

1. *Elastic energy density of the excess term*

Equation (37) is first used to derive the elastic deformation energy density from the excess term in the free energy. Namely, substituting Eq. (37) into the excess term of the free energy, f_{ex} [see Eq. (3)], gives, in reciprocal space,

$$F_{\text{el}}[\hat{n}] = -\sum_{\vec{q}_j} \phi^2_{\vec{q}_j} \hat{C}_2(\vec{q}_j + \vec{q}\,'_j), \tag{38}$$

where $\hat{C}_2$ is rotationally symmetric. The *magnitude* of $\vec{q}_j + \vec{q}\,'_j$ can be written for small $\vec{q}\,'_j$ as $(\vec{q}_j + \vec{q}\,'_j)\cdot(\vec{q}_j/q_j) = q_j + \frac{1}{q_j}(\vec{q}\,'_j\cdot\vec{q}_j)$, where $q_j = |\vec{q}_j|$. This gives

$$F_{\text{el}}[\hat{n}] = -\sum_{\vec{q}_j} \phi^2_{\vec{q}_j} \hat{C}_2\left(q_j + \frac{1}{q_j}(\vec{q}\,'_j\cdot\vec{q}_j)\right). \tag{39}$$

To proceed further, a particular form of $\hat{C}_2(\vec{q})$ must be defined. The common feature of correlation kernels in XPFC models is that they contain peaks in reciprocal space at one or more q values. Each peak i of the correlation kernel can be approximated by a second-order expansion around the peak,

$$\hat{C}^i_2(\vec{q}) \approx A(1 - K(q-k_i)^2 + \ldots). \tag{40}$$

Truncating this expansion at quadratic order and keeping only the peak corresponding to the first mode of the Bravais Fourier series of a BCC lattice (i.e., $i = 1$ with $k_1 = |\vec{q}_{1j}|$) gives, after Eq. (40) is substituted into Eq. (39),

$$F_{\text{el}}[\hat{n}] \approx -\phi^2 A\left[12 - 2Kk_1^2\left(\sum_i \epsilon_{ii}^2 + \sum_{i<j}\left(2\epsilon_{ij}^2 + \epsilon_{ii}\epsilon_{jj}\right)\right)\right], \tag{41}$$

where $\epsilon_{ij} = \epsilon_{ji} = (u_{ij} + u_{ji})/2$ is the infinitesimal strain tensor. For the specific example of the XPFC correlation function in Eq. (14), the expansion around the first peak gives

$$\hat{C}^1_2(\vec{q}) \approx e^{-\frac{\sigma^2 k_1^2}{2\beta_1\rho_1}}\left(1 - \frac{(q-k_1)^2}{\xi_1^2}\right). \tag{42}$$

Comparing Eq. (42) with Eq. (40) gives

$$A = e^{-\frac{\sigma^2 k_1^2}{2\beta_1\rho_1}}, \quad K = \frac{1}{\xi_1^2}. \tag{43}$$

The elastic energy contribution from the excess term becomes

$$\begin{aligned} &F_{\text{el,XPFC}}[\hat{n}] \\ &\approx -\phi^2 e^{-\frac{\sigma^2 k_1^2}{2\beta_1\rho_1}}\left[12 - \frac{2k_1^2}{\xi_1^2}\left(\sum_i \epsilon_{ii}^2 + \sum_{i<j}\left(2\epsilon_{ij}^2 + \epsilon_{ii}\epsilon_{jj}\right)\right)\right]. \end{aligned} \tag{44}$$

2. *Magnetoelastic energy term*

The next step is the calculation of the magnetoelastic free energy. The density expansion of Eq. (35) is substituted into the expression $\vec{m}\cdot\vec{\nabla}n$, which gives

$$\vec{m}\cdot\vec{\nabla}n = \sum_{\vec{q}_j} i\phi_{\vec{q}_j}((\vec{m}\cdot\vec{\nabla})(\vec{u}\cdot\vec{q}_j) + \vec{m}\cdot\vec{q}_j)e^{i\vec{q}_j\cdot(\vec{u}+\vec{r})}. \tag{45}$$

Substituting the above expression into the magnetostriction term of f_m [see Eq. (4)], assuming a BCC lattice for the density expansion, and applying the resonance condition gives

$$\begin{aligned} &f_{\text{me,XPFC}}[\hat{n}] \\ &= \frac{1}{V_u}\int d\vec{r}\left(-\frac{\alpha_2}{2}(\vec{m}\cdot\vec{\nabla}n)^2\right) \\ &\approx -2\alpha_2\phi^2 k_1^2\left(\sum_i m_i^2(1 + 2\epsilon_{ii}) + 4\sum_{i<j} m_i m_j \epsilon_{ij}\right). \end{aligned} \tag{46}$$

Equations (46) and (44) are the basis from which the magnetorestriction coefficients are calculated next.

3. *Calculation of magnetostriction constants*

Following Kittel [54], a cubic system is expected to have a magnetoelastic free energy of the form

$$\begin{aligned} F_{\text{me}} = {}& B_1\sum_i m_i^2\epsilon_{ii} + B_2\sum_{i<j} m_i m_j \epsilon_{ij} + \frac{1}{2}c_{11}\sum_i \epsilon_{ii}^2 \\ &+ 2c_{44}\sum_{i<j}\epsilon_{ij}^2 + c_{12}\sum_{i<j}\epsilon_{ii}\epsilon_{jj}. \end{aligned} \tag{47}$$

When this free energy is minimized with respect to all the strains we obtain the following stress-free strains:

$$\begin{aligned} \epsilon_{ii} &= \frac{B_1}{c_{11} - c_{12}}\left(\frac{|\vec{m}|^2 c_{12}}{c_{11} + 2c_{12}} - m_i^2\right), \\ \epsilon_{ij} &= -\frac{B_2}{4c_{44}} m_i m_j, \quad i \neq j. \end{aligned} \tag{48}$$

The magnetostriction constants λ_{100},λ_{111} are defined by [54]

$$\frac{\delta l}{l}=\frac{3}{2}\lambda_{100}\left(\sum_i \frac{m_i^2\beta_i^2}{|m|^2}-\frac{1}{3}\right)+3\lambda_{111}\sum_{i<j}\frac{m_i m_j\beta_i\beta_j}{|m|^2}, \qquad (49)$$

where $\delta l/l$ is the extension of the sample along the direction of the unit vector $\vec{\beta}$ due to the magnetization. It can be shown that [54]

$$\frac{\delta l}{l}=\sum_{i\leqslant j}\epsilon_{ij}\beta_i\beta_j. \qquad (50)$$

Substituting the solutions from Eq. (48) into Eq. (50), dropping constant terms, and comparing with Eq. (49), we obtain [54]

$$\lambda_{100}=-\frac{2}{3}\frac{B_1|m|^2}{c_{11}-c_{12}},\quad \lambda_{111}=-\frac{1}{12}\frac{B_2|m|^2}{c_{44}}. \qquad (51)$$

Next, comparing Eq. (47) to $F_{\mathrm{el,XPFC}}+F_{\mathrm{me,XPFC}}$ gives

$$\begin{aligned} B_1&=-4\alpha_2\phi^2k_1^2,\quad B_2=-8\alpha_2\phi^2k_1^2,\\ c_{11}&=4\phi^2k_1^2AK,\quad c_{44}=2\phi^2k_1^2AK, \qquad (52)\\ c_{12}&=2\phi^2k_1^2AK,\end{aligned}$$

which then yields from Eq. (51),

$$\lambda_{100}=\frac{4}{3}\frac{\alpha_2}{AK}|m|^2,\quad \lambda_{111}=\frac{1}{3}\frac{\alpha_2}{AK}|m|^2. \qquad (53)$$

It can be seen immediately that $\lambda_{100}=4\lambda_{111}$. Hence it is not possible with a single-peaked correlation kernel to tune λ_{100} and λ_{111} separately in order to match with two experimental values. Indeed, in order to tune the magnetostriction separately in this case, either the elastic anisotropy $c_{44}/(c_{11}-c_{12})$ or the ratio of B_1 to B_2 must be tuned. The above result is a general result of any single-peaked correlation function.

To go beyond the single-peak result, it is necessary to add a second peak to the correlation function, which corresponds to the second BCC mode. Doing so and performing some tedious but straightforward algebra as discussed above using a two-mode density expansion gives

$$\begin{aligned} F_{\mathrm{el,XPFC2}}[\hat{n}]\approx 2\phi_1^2k_1^2\Bigg(&(A_1K_1+2r^2A_2K_2)\sum_i\epsilon_{ii}^2\\ &+A_1K_1\sum_{i<j}(2\epsilon_{ij}^2+\epsilon_{ii}\epsilon_{jj})\Bigg), \qquad (54)\end{aligned}$$

where

$$A_i=e^{-\frac{\sigma^2k_i^2}{2\beta_i\rho_i}},\quad K_i=\frac{1}{\xi_i^2}, \qquad (55)$$

and where $r=\phi_1/\phi_2$, while constant terms have been ignored. Similarly expanding f_m with a two-mode density expansion gives the two-mode magnetoelastic energy to second order:

$$\begin{aligned} &F_{\mathrm{me,XPFC2}}[\hat{n}]\\ &\approx -2\alpha_2\phi_1^2k_1^2(1+r^2)\left(\sum_i m_i^2(1+2\epsilon_{ii})+4\sum_{i<j}m_im_j\epsilon_{ij}\right). \qquad (56)\end{aligned}$$

Comparing $F_{\mathrm{el,XPFC2}}+F_{\mathrm{me,XPFC2}}$ to F_{me} in Eq. (47) gives

$$\begin{aligned} B_1&=-4\alpha_2\phi^2k_1^2(1+r^2),\quad B_2=-8\alpha_2\phi^2k_1^2(1+r^2),\\ c_{11}&=4\phi^2k_1^2(A_1K_1+2r^2A_2K_2), \qquad (57)\\ c_{44}&=2\phi^2k_1^2A_1K_1\quad c_{12}=2\phi^2k_1^2A_1K_1.\end{aligned}$$

Thus the magnetostriction constants now become

$$\lambda_{100}=\frac{4}{3}\frac{\alpha_2(1+r^2)}{A_1K_1+4r^2A_2K_2}|m|^2, \qquad (58)$$

$$\lambda_{111}=\frac{1}{3}\frac{\alpha_2(1+r^2)}{A_1K_1}|m|^2. \qquad (59)$$

So that $\lambda_{100}=4\lambda_{111}(1+4r^2(A_2K_2)/(A_1K_1))^{-1}$. It is noteworthy that although A_1 and A_2 are fixed in the XPFC model, K_1 and K_2 [Eq. (55)] are tunable parameters. The magnetostriction constants can therefore be tuned individually through the addition of higher-order peaks in the XPFC correlation function. Note that A_1, A_2, and r in general depend on the system parameters of temperature (σ) and average density, making the magnetostriction constants functions of temperature and average density. A similar approach could be followed for other crystal symmetries such as FCC.

4. Piezoelectric coefficients in the ferroelectric model

This section summarizes the piezoelectric coefficients of the ferroelectric model, where f_m is neglected. The results are for the case of the PFC correlation in Eq. (13). The details will be left out as the mathematical steps are identical to the ferromagnetic case shown above.

To proceed, the density is once more expanded according to the single-mode expansion in Eq. (33) and substituted into $f_{\mathrm{id}}+f_{\mathrm{ex}}+f_P$, where the excess term is the single peaked expression in Eq. (13), which gives rise to the BCC structure in 3D. Assuming a complex amplitude of the form in Eq. (34) and applying the resonance conditions yields a long wavelength free energy density of the form

$$\begin{aligned} f&=a_2\phi^2-a_3\phi^3+a_4\phi^4+8B^x|\nabla\phi|^2B^l\phi_0^2-\frac{t}{3}\phi_0^3\\ &\quad+\frac{\nu}{4}\phi_0^4+f_{\mathrm{elas}}(\epsilon_{ij},P_i,\phi), \qquad (60)\end{aligned}$$

where ϕ is the single-mode amplitude and ϕ_0 the average density. Here, a_2,a_3,a_4,t,ν are constants, while B^l is the liquid compressibility. The expression $f_{\mathrm{elas}}(\epsilon_{ij},P_i,\phi)$ denotes the elastic free energy density, which is a function of the strains, polarization components and solid order parameter. Minimizing the elastic free energy with respect to the stains, $\partial f_{\mathrm{elas}}/\partial\epsilon_{ij}=0$ gives the following stress free strains:

$$\epsilon_{ii}^0=Q_{11}P_i^2+Q_{12}\sum_{j\neq i}P_j^2,\quad \epsilon_{ij}^0=Q_{44}P_jP_j,\quad i\neq j, \qquad (61)$$

where $Q_{11}=(2\beta_2-3\sigma_2)/B^x$, $Q_{12}=(\sigma_2-2\beta_2)/B^x$, and $Q_{44}=(Q_{11}-Q_{22})/2$. Equation (61) implies that there is a strain whenever there is polarization of a material, a phenomenon known as piezoelectricity. Expanding the elastic term for strains about their stress free values given by Eq. (61)

give the following for the form of the elastic free energy:

$$f_{\rm elas} = \frac{1}{2}C_{11}\sum_{i=1}^{3}\tilde{\epsilon}_{ii}^2 + 2C_{44}\sum_{i=1}^{3}\sum_{j>i}^{3}\tilde{\epsilon}_{ii}\tilde{\epsilon}_{ij} + C_{12}\sum_{i=1}^{3}\sum_{j>i}^{3}\tilde{\epsilon}_{ii}\tilde{\epsilon}_{jj}, \tag{62}$$

where $\tilde{\epsilon}_{ij} \equiv \epsilon_{ij} - \epsilon_{ij}^0$, $C_{11} = 8B^x\phi^2$, and $C_{12} = C_{44} = C_{11}/2$. The form of ferroeletric anisotropy can be obtained by substituting the stress free strains into Eq. (60). This gives an anisotropic free energy of the form

$$f_P = \alpha_1|\vec{P}|^2 + \alpha_{11}\sum_{i=1}^{3}P_i^4 + \sum_{i=1}^{3}\sum_{j>i}^{3}P_i^2P_j^2 + \alpha_{112}\sum_{i=1}^{3}P_i^6 + \alpha_{112}\sum_{i=1}^{3}\sum_{j>i}^{3}P_i^2P_j^4 + \alpha_{123}P_1^2P_2^2P_3^2, \tag{63}$$

where α_1, α_{11}, α_{111}, α_{112}, and α_{123} are constants, related to the parameters of Eq. (5) and listed in Appendix A. Equation (63) is precisely the form of the bulk terms in the traditional Landau-Ginzburg-Devonshire free energies used in standard phase-field models of ferroelectric materials [20,48].

V. NUMERICAL TESTS AND APPLICATIONS OF MODEL

To illustrate how the methods proposed in the previous section capture the essential features of multiferroic materials, several numerical simulations are illustrated here on both ferroelectric and magnetic systems. For simplicity, two-dimensional systems of square or triangular symmetry were considered for both ferroelectric and ferromagnetic simulations. In ferroelectric simulations, triangular symmetry was simulated using usinge Eq. (13) for $\hat{C}_2$, while for ferromagnetic simulations, triangular and square symmetries were simulated using $\hat{C}_2$ in Eq. (14) with one and two peaks, respectively. Ferroelectric coupling will be presented elsewhere.

A. Ferromagnetism in square polycrystalline order

Using a two-dimensional square XPFC correlation with fourfold anisotropy, we tested for magnetic hysteresis and the effects of magnetic fields on grain growth in a pure material. Simulations were carried using Euler's method. The numerical mesh spacing and time steps were $\Delta x = 0.1$ and $\Delta t = 0.001$, respectively. Unless otherwise stated, the parameters used were $(t,v) = (1,1)$, $(W_0,r_m,\omega_m,\gamma_m) = (0.1,0.01,0.4,1)$, $(\xi_1,\xi_2) = (0.9,1.27279)$, $(\rho_1,\rho_2) = (1,\sqrt{2}/2)$, $(\beta_1,\beta_2) = (4,4)$, and $(M_n,\tau_m) = (1,1)$. Other parameters are specified in the text.

1. *Magnetic hysteresis*

We consider here the simplest case of magnetic hysteresis of a perfect crystal, with an alternating magnetic field aligned to the magnetocrystalline easy axis. In this situation, the magnetic free energy can be written in the form

$$f_m(\vec{m}) = f_1(\vec{m}) - \vec{m}\cdot\vec{B}. \tag{64}$$

In general, this free energy will have a number of stationary points defined by $\partial f_m/\partial m_i = 0$. Those which are also local minima will be stable and magnetization can come to rest there. With an external magnetic field present, and oriented in the reverse direction, some local minima can become metastable. Eventually, at high enough external fields, these metastable points become unstable and the magnetization abruptly reverses. Reversing the external field repeats this cycle in the opposite direction. Plotting the magnetization against the external field results in a hysteresis loop, such as the one shown in Fig. 4 for a two-dimensional single square crystal.

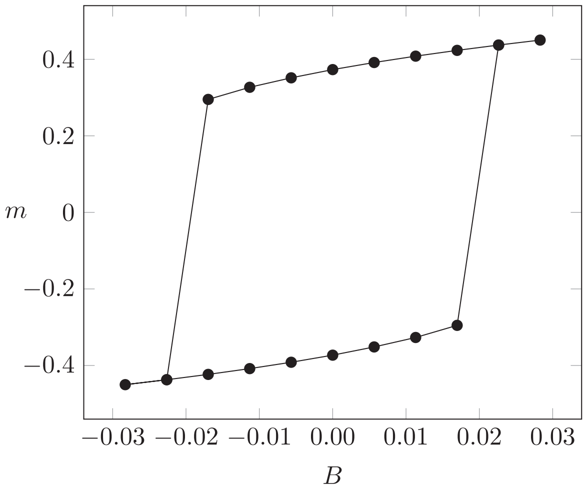

FIG. 4. Hysteresis loop for a single two dimensional square crystal. System parameters are as stated at the beginning of the section with $\sigma = 0.04$, $n_0 = 0.05$, and $(\alpha_2,\alpha_4) = (0.001,-0.01)$.

To produce the hysteresis loop in Fig. 4, the system was brought to magnetic saturation by an initially strong external field. After a set amount of time the process of measuring the hysteresis loop began. The external field was brought through ten successively decreasing values. For each external field value the magnetization was allowed to relax until $d\vec{m}/dt$ was smaller than a convergence value (10^{-5} in Fig. 4), ensuring that the magnetization had reached a local minima corresponding to each value of the external field. The external field was then decreased to its next value. As the strength of the external field increases in the negative direction the magnetization eventually reverses direction. This process gives the drop from the upper left quadrant to the lower left quadrant of the loop in Fig. 4. Once the external field was at its negative extreme the process was reversed and the external field increased at each step back towards its initial value, causing the magnetization to reverse again. This process produces the raise from the lower right to upper right quadrants of the loop in Fig. 4. Figure 5 plots the magnetization (both m_x and m_y) versus time for the entire process. Note that the magnetization reverses by rotation of the magnetization vector.

2. *Solidification under an external field*

The ability to use external magnetic fields to influence the growth of crystal grains has potential applications in microstructural engineering. Here, we consider simulations where crystal seeds of random orientations nucleate, grow, impinge, and coarsen with and without the influence of an

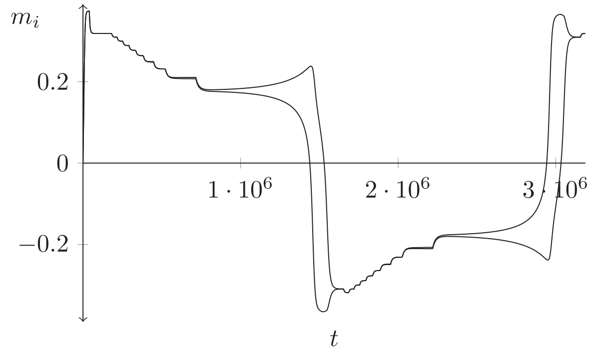

FIG. 5. Plot of magnetization components m_x and m_y vs. time (t) for the hysteresis loop in Fig. 4. Note that the magnetization reverses by rotation of the magnetization vector.

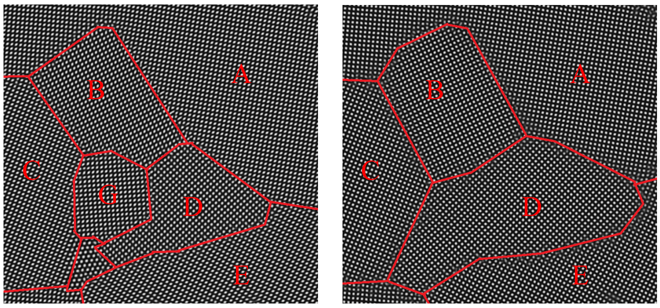

FIG. 7. (Color online) Comparison of initially identical systems grown under an external magnetic field (left) and no field (right). The crystal grains aligned with the x-y axes (such as A and G) have their easy axes aligned with the external field, and grow at the expense of those that are not aligned (such as D).

external field. We simulated a large two-dimensional system $(4000\Delta x \times 4000\Delta x)$ with 160 randomly oriented square seeds. Solidification was initiated following a quench to $\sigma = 0.04$ and $n_0 = 0.05$. $(\alpha_2,\alpha_4) = (0.001,-0.0005)$ and the other parameters are as discussed in the introduction to this section. When present, the magnetic easy axes lie along the diagonals of the unit cell. This sequence is depicted schematically in Fig. 6.

Two simulations are run with the same pseudorandom seed: one with an external field and one without. A snapshot in time of the density field $n(\vec{r},t)$ for the two cases is shown in Fig. 7 for $t = 5.75 \times 10^4 \Delta t$. The red lines mark the polycrystalline grain boundaries in the two cases. In order to investigate the effects of the external field on grain orientation, we computed the power spectrum of the density field n as a function of orientation (θ) at the distance in k space of the first Bragg peak. The difference in these power spectra is depicted in Fig. 8 after 1.4×10^5 time steps. The external field is oriented at an angle of $\theta = \pi/4$; thus a crystal grain oriented with its principle reciprocal lattice vectors along the directions $\theta = 0,\pi/2,\pi,3\pi/2$ will have its easy axes aligned to the external field. Figure 8 shows that a greater portion of grains evolve to become aligned along these angles when the external field is present.

We also compared the power spectra of the same system at late and early times. Figure 9 shows such a comparison for the system with an external field present, where the density field is evaluated at $t_{\text{early}} = 1 \times 10^4 \Delta t$ and $t_{\text{late}} = 1.4 \times 10^5 \Delta t$. From it we can draw the same conclusion as in Fig. 8: the presence of the external field results in preferential growth for those grains with easy axes that are aligned to it.

B. Ferroelectricity in triangular polycrystalline materials

This section presents 2D simulations using the single-peak PFC correlation kernel of Eq. (13), which produces anisotropic ordering. Systems of triangular symmetry are elastically isotropic and the terms $|\vec{P} \cdot \vec{\nabla}|^{2j}$ and $|\vec{P} \times \vec{\nabla}|^{2j}$ do not produce anisotropic terms in $\vec{P}$ if $j < 3$ (unlike the BCC case which produce anisotropy at order $j = 2$). Thus for a minimal two-dimensional model of triangular symmetry to produce anisotropy, at least one term of order $j = 3$ must also be considered. The parameters in all ferroelectric PFC model simulations were zero except, $(B_x,t,v) = (1,1,1)$, $(\sigma_2,\sigma_6) = (0.14,0.012)$, $(\gamma_6,\gamma_8) = (-0.006,0.0064)(r_p,\omega_p) = (0.002,0.08)$, and $G_2 = 0.4$. The simulations were conducted on a periodic system with grid spacing $\Delta x = 0.78438$ and time step $\Delta t = 0.2$. Equations (22) and (19) were solved using semispectral methods.

1. *Piezoelectric effect*

To show the piezoelectric effect, a single crystal in equilibrium with a liquid phase with average density difference $n_0 = -0.03$ was subjected to an electric field in several different orientations with magnitude of $|\vec{E}| = 0.005$. The model parameters were chosen such that in the absence of applied fields the equilibrium state is nonferroelectric (i.e., above the transition temperature). When no field is applied, a small crystal forms a roughly hexagonal shape and the lattice has triangular symmetry as shown in Fig. 10(a). When the

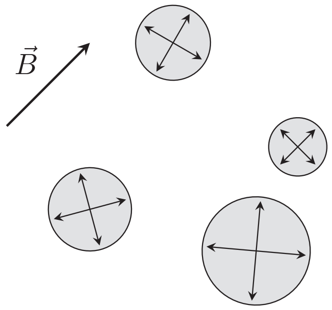

FIG. 6. Randomly oriented crystal seeds growing under the influence of an external field.

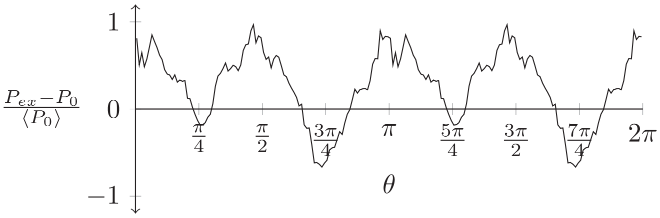

FIG. 8. Difference in power spectra of a polycrystalline solid grown in an external field (P_{ex}) and no external field (P_0), respectively.

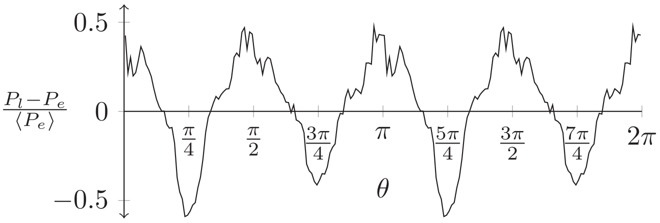

FIG. 9. Difference in power spectra of a polycrystalline solid grown in an external field at late (P_l) and early (P_e) times, respectively.

electric field is applied, the crystal polarizes such that the polarization field is in the opposite direction of the applied field to minimize electric field energy. The polarization in turn induces an elastic strain in the crystal as shown in Figs. 10(b)–10(d).

The displacements of the atomic positions after the field is applied can be seen by comparing the locations of the density maxima with respect to the superimposed white hexagon in this figure. In the absence of an applied field, the maxima lie on the hexagon as shown in Fig. 10(a). This polarization/elastic coupling is the piezoelectric effect. Similar behavior also was observed when a magnetic field is applied, as shown in a prior publication [44,45] for an isotropic variant of the ferromagnetic model presented here. Thus the model presented in the previous section naturally incorporates the piezoelectric effect and magnetostriction. It also is interesting to note that the overall crystal shape changes, such that it elongates in the direction of zero strain (i.e., perpendicular to the applied field).

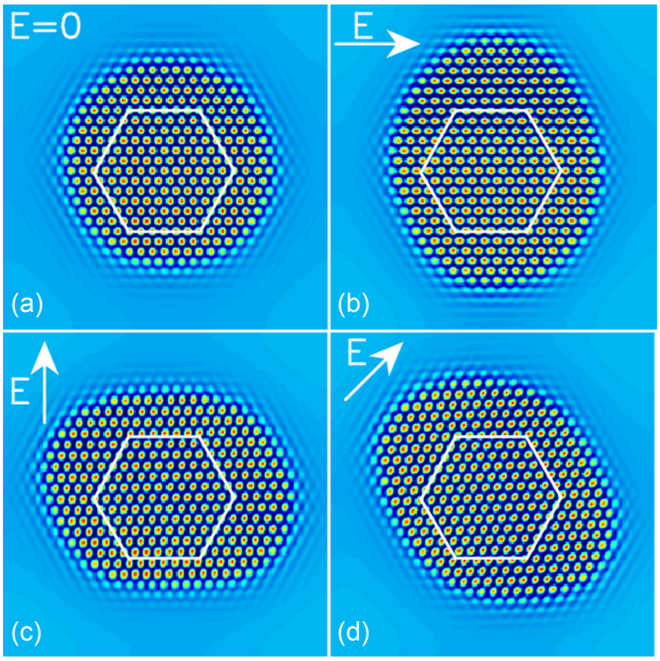

FIG. 10. (Color online) Piezoelectric effect. In this figure, an electric field is applied to a single crystal coexisting with the liquid phase. The color is proportional to n and the direction of the field is indicated in each figure. The same white hexagon is superimposed on each crystal to highlight the displacement of the atomic locations after the external electric field is applied.

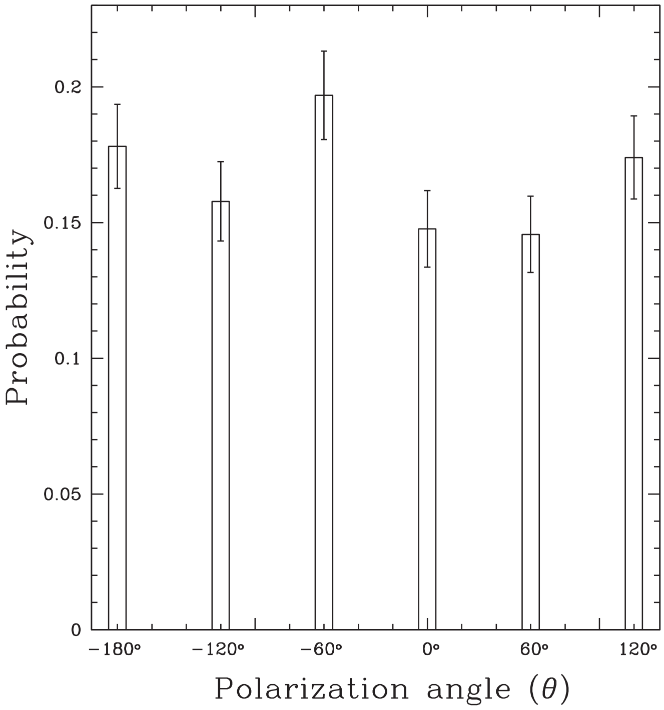

FIG. 11. Anisotropic ordering. The probability of the $\vec{P}$ aligning in a given polarization direction, θ is shown. Ordering occurs at multiples of 60° consistent with the symmetry of a two-dimensional triangular lattice.

2. *Anisotropic ordering*

As discussed previously, when a material undergoes a ferroelectric or ferromagnetic transition, the orientation of $\vec{P}$ and $\vec{m}$ are often determined by the anisotropy of the crystalline lattice. This anisotropic ordering plays a large role in determining, for example, the electric and magnetic coercivity in polycrystalline materials [2–6]. To show that anisotropic ordering occurs and to verify the approximate analytic calculations, simulations were conducted below the ferroelectric transition in a periodic simulation cell. For these simulations the initial condition was a small perfect single crystal in an orientation and under conditions consistent with Fig. 10(a), and random fluctuations for the polarization field, $\vec{P}$. The dynamical equations were evolved until the equilibrium was reached. Approximately 800 different initial conditions were run and the equilibrium polarization direction was calculated for each run. A histogram of the final orientations is shown in Fig. 11. It is important to note that the selection of the polarization directions, 0°, 60°, 120°, etc., were due to the orientation of the crystal. If the initial crystal was rotated by 10° then the polarization directions would be 10°, 70°, 130°, etc. These simulations clearly show that the easy directions for the polarization field are determined by the crystal lattice.

Simulations of polycrystalline samples also were conducted to show that each grain will select a polarization direction determined by the orientation of the individual grains. Results of the simulations are shown in Fig. 12, which shows a sequence of heterogeneous nucleation, growth and impingement at an average density $n_0 = -0.005$ and quench temperature parameter $\Delta B = 0$. It is seen that each

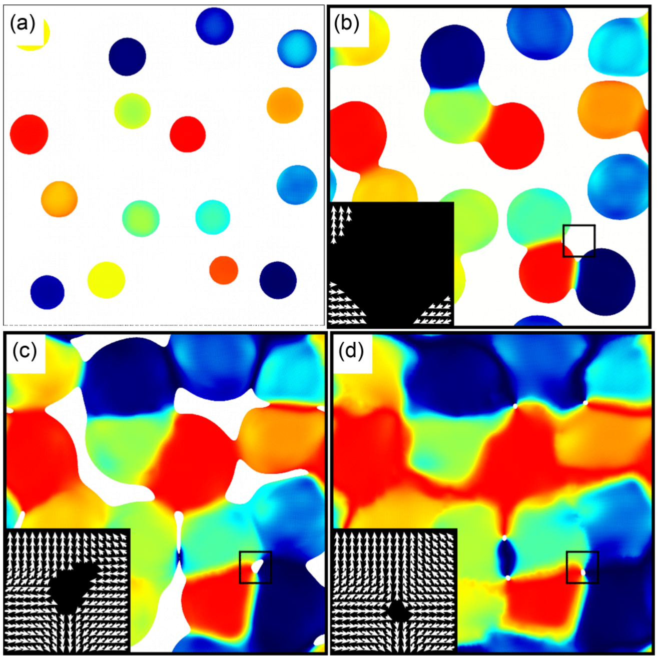

FIG. 12. (Color online) Heterogenous polycrystal nucleation, growth, and impingement from a supercooled melt. In each figure, the color is proportional to the orientation angle of the polarization field within a grain. The inset in (b), (c), and (d) shows the polarization vector for the region inscribed by the black square. The number of time steps following the initial condition in (a), (b), (c), and (d) are 200,300, 400, and 1000, respectively. Defects in the polarization field are marked by small white dots and a rapidly change orientation.

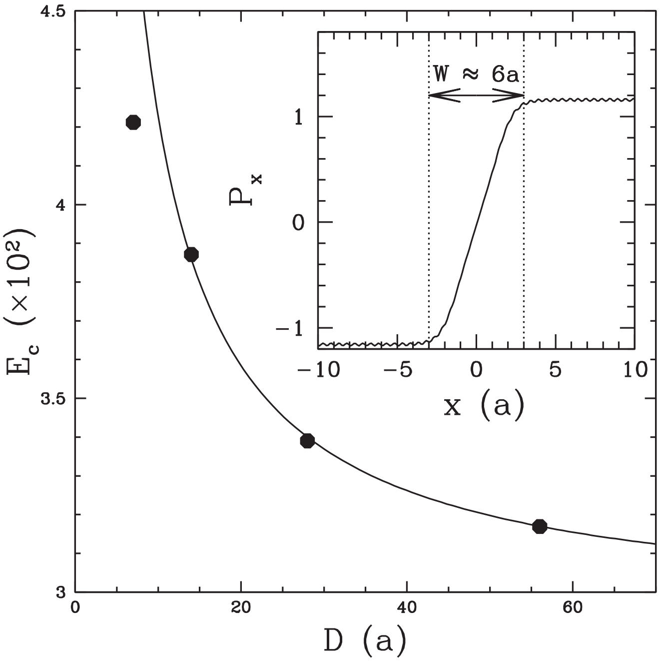

FIG. 13. Coercivity as a function of grain diameter D, expressed in terms of the atomic spacing a. The coercivity E_c is half the width of the hysteresis loops at $P_x = 0$. The line is a fit to $E_c = E_c^0 + A/D$. In the inset, $P_x(x)$ is plotted as a function of position across a 180° domain wall in a single-crystal system.

grain chooses a single orientation after nucleation. If two or more grains impinge with different polarization directions, defects in the polarization field can appear. An example is highlighted in the inset of Fig. 12, which shows the emergence of a point defect after four grains impinge. This typical simulation illustrates the robustness of the multiferroic PFC to model polycrystalline materials in which the easy axes for polarization are determined by the local crystal orientation.

3. *Ferroelectric coercivity*

The magnetic coercivity H_c is strongly correlated with the grain size D in polycrystalline samples such that $H_c \sim D^6$ for small grain size and $H_c \sim 1/D$ for large grains, where the crossover occurs when D is the size of the magnetic exchange length L_{ex}. Both behaviors have been theoretically attributed to the anisotropic ordering of the magnetization field [2–6]. Since it is the anisotropic nature of the ordering that is responsible for such behavior it is expected that similar behavior will occur in ferroelectric systems. To examine the $1/D$ behavior, the exchange length must be much smaller than the grain size. To examine this phenomena, simulations were conducted on a polycrystalline system containing four grains of different orientation. In these simulations, four seeds, of orientations $\theta = 22.3^\circ, 12.2^\circ, 6.7^\circ$, and -19.9°, were introduced into a supercooled melt at zero electric field using the same parameters as in the preceding simulation of polycrystalline growth (Fig. 12). The systems were evolved for a time of $t = 2000$ at which time a polycrystalline sample was formed. The systems were then subjected to a time dependent external electric field. The dynamics of the n were stopped to avoid grain coarsening during the simulation. The electric coercivity E_c was then measured as a function of the system size, as the size was increased (which increases the diameter D of each grain). A plot of E_c versus D is shown in Fig. 13. The inset of this figure shows the behavior of P_x across a 180° domain wall in a single crystal system, indicating a ferroelectric exchange length of approximately $W \approx 6a$. As can be seen in this plot, $E_c \sim 1/D$ for large-sized grains and some deviations occur for the smallest grain diameter ($D \sim 14a$) as expected since $D/2 \approx W$.

VI. DISCUSSION AND CONCLUSIONS

This work presented a new multiferroic phase-field crystal (PFC) model that enables the study of anisotropic magneto/electro-crystalline interactions, which can be simulated alongside the usual elastic, plastic, and thermodynamic driving forces that dictate the formation of complex microstructures in complex multiferroic materials.

The model presented here extends the magnetic phase-field crystal model developed by Faghihi *et al.* [44,45] in two important ways. First, it adds the capability to simultaneously model both ferromagnetism and ferroelectricity, as well as coupling between the two phenomena. Second, this work introduced new magnetic/density (or ferroelectric/density) couplings in the free energy functional (i.e., $(\vec{m} \cdot \vec{\nabla} n)^{2j}$, $|\vec{P} \cdot \vec{\nabla} n)|^{2j}$, and $|\vec{P} \times \vec{\nabla} n)|^{2j}$). These couplings were shown analytically and numerically to induce anisotropic ordering of the magnetic and polarization fields. Namely, it was shown that

TABLE III. Normalized reciprocal lattice vectors used in calculations.

Lattice	Mode	Vectors
BCC	1	$\{(1,1,0), (1,0,-1), (0,1,-1), (1,0,1), (1,-1,0), (0,1,1), (0,-1,-1),$ $(-1,1,0), (-1,0,-1), (0,-1,1), (-1,0,1), (-1,-1,0)\}$
	2	$\{(2,0,0), (0,2,0), (0,0,-2), (0,0,2), (0,-2,0), (-2,0,0)\}$
HCP	1	$\{(0,0,1), (0,0,-1)\}$
	2	$\left(\frac{4\sqrt{2}}{3}\right)\{(1,0,0), \left(\frac{1}{2},-\frac{\sqrt{3}}{2},0\right), \left(\frac{1}{2},\frac{\sqrt{3}}{2},0\right), \left(-\frac{1}{2},-\frac{\sqrt{3}}{2},0\right), \left(-\frac{1}{2},\frac{\sqrt{3}}{2},0\right), (-1,0,0)\}$

the local crystal orientation alone determines the local ordering directions of the magnetic and polarization fields. This is a critical feature that influences many physical properties of multiferroic materials.

The long-wavelength properties of the model were also examined and shown to self-consistently reproduce the physical features associated with magnetostriction and the piezoelectric effect. Specifically, the magnetostriction and piezoelectric coefficients were derived and their form was connected to the multipeaked structure of the two-point correlation kernel used in the PFC excess free energy. Notably, it was found that with a two-peaked PFC correlation kernel, it is possible to arbitrarily control the value of these two coefficients. The forms of the long wavelength limit of the two cases of the model studied were found to be the same as those used in phenomenological multiferroic phase-field models in the literature.

The present work can be extended in several important ways. On the applications side, since the phase-field crystal model incorporates elastoplasticity in polycrystalline materials, it can be used to examine the role of external magnetic or electric fields on the evolution of defect structures, on diffusion time scales. In effect, this can open a window into the exploration of *microstructure engineering* via low level external fields in multiferroic materials. Another interesting direction is the use of coarse graining techniques such as those presented elsewhere [39,40,43,55] to derive novel multiferroic phase-field models based on complex order parameters. Such models naturally incorporate grain boundaries, elasticity, and some dislocation properties. It is noteworthy that such models are immune from the CPU limitation of traditional multiphase-field models, which require as many order parameters at crystal grains (or phases in the case of an alloy). In this case, an arbitrary number of crystal orientations and phases could be modelled by a single complex order parameter. This will be the topic of upcoming publications.

APPENDIX A: ANISOTROPIC FERROELECTRIC FREE ENERGY COEFFICIENTS

The values of the coefficients that go into Eq. (63) are

$$\begin{aligned}
\alpha_1 &= \frac{r_p}{2} + \phi^2(8\beta_2 + 4\sigma_2 - 3\omega_p),\\
\alpha_{11} &= \frac{\nu_4}{4} + \phi^2\left(\phi^2(54\sigma_4 + 130\beta_4) + \frac{4}{B^x}(2\beta_2 + \sigma_2)^2\right),\\
\alpha_{12} &= \frac{\nu_4}{2} + \phi^2\Bigg(\phi^2(66\sigma_4 + 218\beta_4)\\
&\quad + \frac{24}{B^x}\left(4\beta_2^2 - 4\beta_2\sigma_2 + 3\sigma_2^2\right)\Bigg), \qquad \text{(A1)}\\
\alpha_{111} &= \frac{\nu_6}{6} + \frac{\phi^6}{3}(4000\sigma_6 + 10640\beta_2),\\
\alpha_{112} &= \frac{\nu_6}{2} + 8\phi^6(275\sigma_6 + 1061\beta_6),\\
\alpha_{123} &= \nu_6 + 16\phi^6(835\sigma_6 + 924\beta_6).
\end{aligned}$$

APPENDIX B: RECIPROCAL LATTICE VECTORS

Table III lists the reciprocal lattice vectors used in amplitude expansion calculations [56].

[1] A. Hubert and R. Schafer, *Magnetic Domains The Analysis of Magnetic Microstructures* (Springer-Verlag, Berlin, 1998).

[2] G. Herzer, *Nanocrystalline Soft Magnetic Alloys* (Elsevier, Amsterdam, 1997), Chap. 3.

[3] G. Herzer, IEEE Trans. Magn. **26**, 1397 (1990).

[4] G. Herzer, Scripta Metel. et Mater. **33**, 1741 (1995).

[5] G. Herzer and H. Warlimont, Nanostruct. Mater. **1**, 263 (1992).

[6] F. Pfeifer and C. Radeloff, J. Magn. Magn. Mater. **19**, 190 (1980).

[7] M. Mekhiche, T. Waeckerle, F. Ossart, and T. Pera, IEEE Trans. Magn. **31**, 3554 (1995).

[8] T. Tomida, N. Sano, S. Hinotani, K. Fujiwara, H. Kotera, N. Nishiyama, and Y. Ikkai, IEEE Trans. Magn. **41**, 4063 (2005).

[9] G. Lawes and G. Srinivasan, J. Phys. D: Appl. Phys. **44**, 243001 (2011).

[10] D. Chiba, M. Sawicki, Y. Nishitani, Y. Nakatani, F. Matsukura, and H. Ohno, Nat. Lett. **455**, 515 (2008).

[11] T. H. E. Lahtinen, J. O. Tuomi, and S. van Dijken, Adv. Mater. **23**, 3187 (2011).

[12] T. H. E. Lahtinen, J. O. Tuomi, and S. van Dijken, IEEE Trans. Magn. **47**, 3768 (2011).

[13] J. Boomgaard, D. R. Terrell, R. A. J. Born, and H. F. J. I. Giller, J. Mater. Sci. **9**, 1705 (1974).

[14] A. M. J. G. Run, D. R. Terrell, and J. H. Scholing, J. Mater. Sci. **9**, 1710 (1974).

[15] J. Boomgaard, A. M. J. G. Run, and J. Suchtelen, Ferroelectrics **10**, 295 (1976).

[16] B. Echebarria, R. Folch, A. Karma, and M. Plapp, Phys. Rev. E **70**, 061604 (2004).

[17] N. Provatas, N. Goldenfeld, and J. Dantzig, Phys. Rev. Lett. **80**, 3308 (1998).
[18] N. Provatas, J. Dantzig, and N. Goldenfeld, J. Comput. Phys. **148**, 265 (1999).
[19] A. F. Devonshire, Philos. Mag. **3**, 85 (1954).
[20] S. Choudhury, Y. L. Li, C. Krill III, and L. Q. Chen, Acta. Mater. **55**, 1415 (2007).
[21] K. R. Elder and M. Grant, Phys. Rev. E **70**, 051605 (2004).
[22] P. Stefanovic, M. Haataja, and N. Provatas, Phys. Rev. Lett. **96**, 225504 (2006).
[23] K. R. Elder, N. Provatas, J. Berry, P. Stefanovic, and M. Grant, Phys. Rev. B **75**, 064107 (2007).
[24] K. R. Elder, M. Katakowski, M. Haataja, and M. Grant, Phys. Rev. Lett. **88**, 245701 (2002).
[25] M. Greenwood, N. Provatas, and J. Rottler, Phys. Rev. Lett. **105**, 045702 (2010).
[26] W. H. Shih, Z. Q. Wang, X. C. Zeng, and D. Stroud, Phys. Rev. A **35**, 2611 (1987).
[27] T. V. Ramakrishnan and M. Yussouff, Phys. Rev. B **19**, 2775 (1979).
[28] Y. M. Jin and A. G. Khachaturyan, J. Appl. Phys. **100**, 013519 (2006).
[29] K.-A. Wu, A. Adland, and A. Karma, Phys. Rev. E **81**, 061601 (2010).
[30] K.-A. Wu, M. Plapp, and P. W. Voorhees, J. Phys. Condens. Matter **22**, 364102 (2010).
[31] S. K. Mkhonta, K. R. Elder, and Z.-F. Huang, Phys. Rev. Lett. **111**, 035501 (2013).
[32] M. Greenwood, N. Ofori-Opoku, J. Rottler, and N. Provatas, Phys. Rev. B **84**, 064104 (2011).
[33] N. Ofori-Opoku, V. Fallah, M. Greenwood, S. Esmaeili, and N. Provatas, Phys. Rev. B **87**, 134105 (2013).
[34] J. Berry, N. Provatas, J. Rottler, and C. W. Sinclair, Phys. Rev. B **86**, 224112 (2012).
[35] J. Berry, N. Provatas, J. Rottler, and C. W. Sinclair, Phys. Rev. B **89**, 214117 (2014).
[36] V. Fallah, N. Ofori-Opoku, J. Stolle, N. Provatas, and S. Esmaeili, Acta Mater. **61**, 3653 (2013).
[37] V. Fallah, A. Korinek, N. Ofori-Opoku, N. Provatas, and S. Esmaeili, Acta Mater. **61**, 6372 (2013).
[38] V. Fallah, A. Korinek, N. Ofori-Opoku, B. Raeisinia, M. Gallerneault, N. Provatas, and S. Esmaeili, Acta Mater. **82**, 457 (2015).
[39] K. R. Elder, Z.-F. Huang, and N. Provatas, Phys. Rev. E **81**, 011602 (2010).
[40] Z.-F. Huang, K. R. Elder, and N. Provatas, Phys. Rev. E **82**, 021605 (2010).
[41] K.-A. Wu and A. Karma, Phys. Rev. B **76**, 184107 (2007).
[42] N. Provatas and S. Majaniemi, Phys. Rev. E **82**, 041601 (2010).
[43] N. Ofori-Opoku, J. Stolle, Z.-F. Huang, and N. Provatas, Phys. Rev. B **88**, 104106 (2013).
[44] N. Faghihi, Ph.D. Thesis, The University of Western Ontario, 2012.
[45] N. Faghihi, N. Provatas, K. R. Elder, M. Grant, and M. Karttunen, Phys. Rev. E **88**, 032407 (2013).
[46] M. Greenwood, J. Rottler, and N. Provatas, Phys. Rev. E **83**, 031601 (2011).
[47] P. P. Wu, X. Q. Ma, J. X. Zhang, and L. Q. Chen, Philos. Mag. **90**, 125 (2010).
[48] G. B. Stephenson and K. R. Elder, J. Appl. Phys. **100**, 051601 (2006).
[49] M. J. Haun, E. Furman, S. J. Jang, H. A. McKinstry, and L. E. Cross, J. Appl. Phys. **62**, 3331 (1987).
[50] M. J. Haun, Z. Z. E. Furman, S. J. Jang, and L. E. Cross, Ferroelectrics **99**, 45 (1989).
[51] A. Jaatinen, C. V. Achim, K. R. Elder, and T. Ala-Nissila, Phys. Rev. E **80**, 031602 (2009).
[52] A. Jaatinen and T. Ala-Nissila, Phys. Rev. E **82**, 061602 (2010).
[53] H. Humadi, J. Hoyt, and N. Provatas, Phys. Rev. E **87**, 022404 (2013).
[54] C. Kittel, Rev. Mod. Phys. **21**, 541 (1949).
[55] R. Spatschek and A. Karma, Phys. Rev. B **81**, 214201 (2010).
[56] C. Kittel, *Introduction to Solid State Physics* (Wiley, New York, 2005).